Collective blade pitch angle effect on grid turbulence ingestion noise by an isolated propeller

Quaroni, L.N.; Merino Martinez, R.; do Nascimento Monteiro, F.; KUMAR, S.

DOI
10.2514/6.2024-3209

Publication date
2024

Document Version
Final published version

Published in
30th AIAA/CEAS Aeroacoustics Conference (2024)

Aeroacoustics Conferences
June 4-7, 2024, Rome, Italy
30th AIAA/CEAS Aeroacoustics Conference (2024)

10.2514/6.2024-3209

Collective blade pitch angle effect on grid turbulence ingestion noise by an isolated propeller

Luca Nicola Quaroni*, Roberto Merino-Martínez†, Fernanda do N. Monteiro ‡ and S. Satish Kumar §
Faculty of Aerospace Engineering, Delft University of Technology, 2629 HS Delft, the Netherlands

An experimental aeroacoustic study on the influence of the collective blade pitch angle in the noise emissions by an isolated propeller under different turbulent inflow conditions is presented. Acoustic and aerodynamic measurements are conducted in an anechoic, open-jet wind tunnel facility. Different inflow turbulence characteristics are achieved by employing square-mesh, square-bar turbulence grids positioned ahead of an additional 2:1 contraction at the wind tunnel's exit. It is found that the ingestion of grid-generated turbulence does not significantly impact the thrust produced by the propeller for any of the tested collective blade pitch angles. On the other hand, turbulence ingestion greatly increases noise production in both broadband and tonal components. The grouping of broadband noise around the Blade Passing Frequency (BPF) and its harmonics ("haystacking") does not prove to be a phenomenon of particular relevance in grid-generated turbulence ingestion. A directivity analysis shows that an increase in inflow turbulence intensity is responsible for increased noise emissions downstream of the propeller.

Nomenclature

A_{wt}	=	wind tunnel exit nozzle area, [m^2]
A_{ext}	=	additional contraction exit area, [m^2]
A_p	=	propeller area, [m^2]
B	=	number of blades, [-]
c_0	=	speed of sound, [m/s]
c	=	airfoil chord, [m]
C_{p_t}	=	total pressure coefficient, [-]
d	=	grid bar width, [m]
D_p	=	propeller diameter, [m]
D_{wt}	=	wind tunnel exit nozzle diameter, [m]
D_{ext}	=	additional contraction exit nozzle diameter, [m]
D_{cntr}	=	additional contraction diameter, [m]
h	=	streamwise distance between propeller disk plane and contraction's exit, [m]
L	=	additional contraction length, [m]
M	=	grid mesh width, [m]
$\bar{M}$	=	freestream Mach number, [-]
J	=	advance ratio, [-]
p_t	=	total pressure, [Pa]
q_∞	=	freestream dynamic pressure, [Pa]
$R_{0.7R_p}$	=	chord-based Reynolds number at 70% of blade's radius, [-]
R_p	=	propeller radius, [m]
R_h	=	propeller's hub radius, [m]
R_n	=	nacelle's radius, [m]
T	=	thrust, [N]

*Corresponding author, Postdoctoral researcher, Aircraft Noise and Climate Effects (ANCE), L.N.Quaroni@tudelft.nl
†Assistant professor, Aircraft Noise and Climate Effects (ANCE), r.merinomartinez@tudelft.nl
‡PhD candidate, Wind Energy, f.donascimentomonteiro@tudelft.nl
§Raman research fellow, Sustainable Aircraft Propulsion, s.kumar-4@tudelft.nl

T_c	=	thrust coefficient, [−]
TI	=	turbulence intensity, [%]
$TSSPL$	=	thrust-scaled sound pressure level, [dB/Hz]
$\bar{V}$	=	average streamwise velocity, [m/s]
v'	=	fluctuating streamwise velocity, [m/s]
x	=	streamwise coordinate starting from wind tunnel exit, [m]
β	=	grid porosity, [−]
β_c	=	collective blade pitch angle, [°]
$\beta_{0.7R_p}$	=	blade pitch angle at 70% of blade's radius, [°]
Δp_t	=	total pressure rise across propeller's disk, [Pa]
Λ_x	=	streamwise integral turbulence length scale, [m]
ρ	=	air density, [kg/m^3]
χ	=	haystacking parameter, [-]
ν	=	kinematic air viscosity, [m^2/s]
BLI	=	Boundary Layer Ingestion
BPF	=	Blade Passage Frequency
CFDBF	=	Conventional Frequency Domain Beamforming
BPF	=	Blade Passing Frequency
ESC	=	Electronic Speed Controller
HWA	=	Hot Wire Anemometry
TIN	=	Turbulence Ingestion Noise
UAV	=	Unmanned Aerial Vehicle
UAM	=	Urban Air Mobility

I. Introduction

Propeller noise has recently been attracting the attention of researchers due to both an increased awareness of noise pollution and the rise of novel propulsive technologies involving the use of propellers. Amongst such technologies, one may cite the rapid development of unmanned aerial vehicles (UAVs), distributed electric propulsion concepts, and the introduction of boundary layer ingestion (BLI) systems in aircrafts, whereby a distorted inflow is fed to the propeller for increased propulsive efficiency [1]. Concerning the latter, several configurations have been suggested (e.g. over-the-wing- and aft-installed propellers), with the common characteristic of turbulence ingestion [2]. Whilst beneficial for an overall drag reduction, this leads to undesired additional noise, usually referred to as Turbulence Ingestion Noise (TIN).

The vortical structures present in a turbulent flow interact with a propeller's blades by being "chopped" as they pass through the propeller's rotational plane. The resulting unsteady loading of the blade section that the vortex has come in contact with then translates into an increase in the broadband noise emissions [3]. Moreover, if the ingested structures are sufficiently elongated in the stream-wise direction, a single vortex can be "chopped" multiple times at the blade passing frequency (BPF) [4]. This "chopping" of the same vortex by subsequent blades induces a correlation between the pressure fluctuations acting on the blades' surfaces, leading to a regrouping of the broadband noise into "humps" centered at the BPF and its harmonics, a phenomenon also known as "haystacking" [5, 6]. This may further exacerbate the typically tonal nature of propeller noise emissions. A convenient criterion for the occurrence of "haystacking" is given by [7]:

$$\chi = \frac{B\Omega\Lambda_x}{\bar{V}} \gg 1 \tag{1}$$

where χ is the so-called "haystacking" parameter, B is the number of blades, Ω is their angular velocity, Λ_x is the streamwise integral length scale of the turbulence field ingested by the propeller, and $\bar{V}$ is the average streamwise velocity.

The present study discusses the results of an experimental aeroacoustic wind-tunnel investigation of TIN from grid-generated turbulence interacting with a six-bladed propeller at low tip Mach numbers. The main objective of the campaign was to evaluate the influence of the collective blade pitch angle β_c of the propeller's blades on the far-field noise emissions due to the interaction of the propeller with nearly-isotropic turbulent inflows of varying turbulence integral length scales. While several studies on TIN employing grid-generated turbulence are present in the literature (e.g. [8, 9]), a thorough investigation of the effect of the blades' collective blade pitch angle on the noise emissions is currently lacking to the best of the authors' knowledge and would, therefore, be an addition to the body of knowledge on the subject. This investigation is expected to be of special interest for realistic scenarios with varying blade pitch angle operational conditions, such as BLI systems or urban air mobility (UAM) vehicles.

In Sec. II the experimental setup (wind tunnel facility and test rig) used in the experimental campaign, as well as the test conditions, are described. Section III summarizes and discusses the aerodynamic and acoustic experimental results obtained, whereas Sec. IV gathers the main conclusions from this study.

II. Experimental set-up and test conditions

A. Wind tunnel facility

The experiments are performed at the anechoic vertical wind tunnel facility, also known as the A-Tunnel, of Delft University of Technology (TU Delft). The facility has an open-jet test section in a closed-circuit configuration. Air is drawn from a settling chamber at the ground floor through an axisymmetric contraction with a 15:1 area ratio into an anechoic plenum at the first floor of approximately 6.4 m × 6.4 m floor area and 3.2 m in height. Acoustic absorbing foam wedges placed on the walls, ceiling, and floor of the plenum allow for free-field sound propagation for frequencies above 200 Hz. The wind tunnel's circular contraction has an exit diameter D_{wt} of 0.6 m and allows for additional nozzles to be flanged at its top. With no additional contractions, the maximum velocity that can be reached is 35 m/s with an overall maximum turbulence intensity at the jet's core lower than 0.22%. For a more in-depth description of the facility, the reader is referred to Merino-Martinez *et al.* [10].

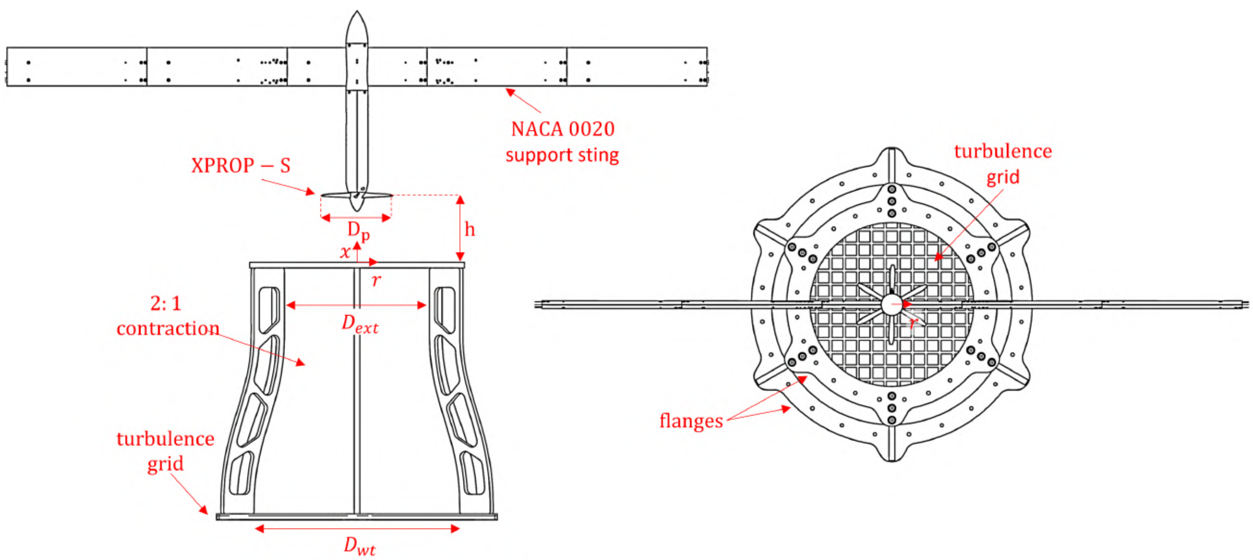

Fig. 1 Side (left) and top (right) rendering of the test rig.

B. Test rig

The current study employed an isolated six-bladed steel propeller placed within the open-jet test section, set perpendicularly to the flow (i.e. at zero-yaw angle). The model propeller, referred to as XPROP-S, has already been extensively studied in several previous publications focusing on its aerodynamic and performance characteristics [11, 12]. It has a diameter D_p of 0.2032 m, featuring blade profiles of Clark-Y airfoil type with a trailing edge thickness of 0.2 mm. The collective blade pitch angle can be manually set to an accuracy of ± 0.05°. The propeller is driven by a brushless DC electrical motor able to attain rotational velocities of up to 12,000 RPM while a rotary optical encoder mounted on the rotor shaft allows for the reading of the motor's effective RPM. The propeller was mounted on an aluminum nacelle (R_n = 56 mm) fixed to a straight support sting with a NACA 0020 airfoil profile of 100 mm chord, truncated at the last

2 mm of the chord at the trailing edge for manufacturing purposes. Carborundum grain strips were positioned at both leading edges of the supporting sting and around the nacelle immediately downstream of the propeller to promote the transition of the boundary layer from laminar to turbulent [13], reducing the risk of laminar vortex shedding. The sting was then clamped at its ends to a support structure connected to the plenum chamber's floor to center the propeller with respect to the jet axis and the wind tunnel's exit, see Figure 1.

Three different turbulence grids with constant porosity $\beta = ((M - d)/M)^2 = 0.64$ and different square mesh lengths M and bar widths d were manufactured by water-cutting an aluminum plate of 5 mm thickness to obtain a planar grid structure (see Fig. 2 and Table 1). The choice of keeping a constant porosity for different mesh sizes was taken to ensure different axial integral turbulence length scales Λ_x for relatively similar values of turbulence intensities [14]. An additional contraction to be inserted between the grids and the propeller was also designed for improving the isotropy of the generated turbulent flow, reducing the grids' self-noise and attaining higher inflow velocities to the propeller [15, 16]. The new contraction features a fifth-order polynomial contour as suggested by Bell & Mehta [17]:

$$D_{cntr}(x) = D_{wt} + (D_{wt} - D_{ext})\left[-10\left(\frac{x}{L}\right)^3 + 15\left(\frac{x}{L}\right)^4 - 6\left(\frac{x}{L}\right)^5\right], \tag{2}$$

where the nozzle length L is set to 0.48 m ($L/D_{cntr} = 0.8$) and the exit nozzle diameter D_{ext} to 0.42 m to achieve a 2:1 area ratio A_{wt}/A_{ext}. An additional straight cylindrical segment with a length of $D_{wt}/2$ was added after the contracting part of the nozzle to improve flow uniformity at its exit [18]. The contraction was manufactured by 3D printing. A rendering of the test-rig is provided in Fig. 1, in which the propeller is at a distance h from the contraction's exit. To ensure that the propeller is fully contained within the exit jet's potential core, the value of h should be within one outlet nozzle diameter D_{ext} [16]. For the current study h was set to $0.4D_{ext}$, see Sec.III.A.

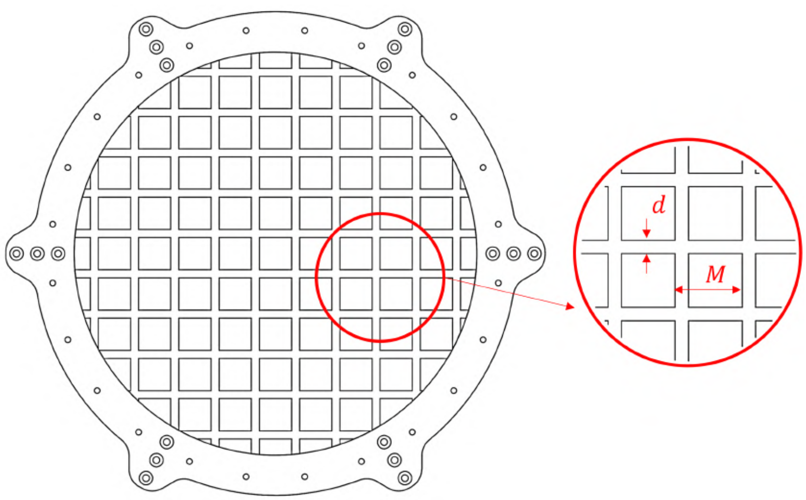

Fig. 2 Flanged turbulence grid and detail view with indication of mesh length M and bar width d.

C. Measurement techniques

The experimental campaign included both aerodynamic and acoustic measurements.

1. Aerodynamic measurements

The freestream velocity $\bar{V}$ at the exit of the contraction was obtained by measuring the pressure difference developed between the settling chamber of the wind tunnel facility and the anechoic plenum, following the calibration of the full wind tunnel section (i.e. with the new contraction flanged at the end of the standard wind tunnel's exit) using a Pitot tube. A digital 7-hole pressure probe system (Surrey Sensors IDXHP-6K9) was employed to retrieve the average total pressure distribution p_t and the velocity components (axial V_{ax}, tangential/swirl V_θ and radial V_r) in the propeller's slipstream. A 90°-bend probe allowed for side-way access to the measurement plane with minimal intrusion. The probe tip was

Table 1 Porosity β, bar width d and mesh length M of the aluminum grids. Additionally reported are the turbulence intensity TI and the streamwise turbulent integral length scale Λ_x at a distance $x = 0.4D_{ext}$ downstream of nozzle exit for a freestream velocity of 30 m/s.

Grid	β	d	M	TI	Λ_x
[-]	[%]	[mm]	[mm]	[%]	[mm]
A	64	7	35	1.97	11.4
B	64	10	50	2.75	14.1
C	64	12	60	3.44	16.2

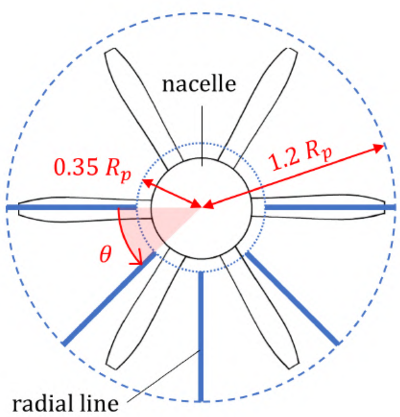

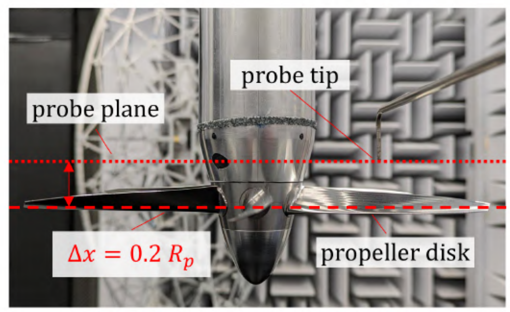

Fig. 3 Schematic of radial lines traversed by 7-hole pressure probe as seen from downstream of the propeller (left) and lateral view of the relative position of the measurement plane with respect to the propeller (right).

positioned at a distance of 0.2 R_p downstream of the propeller disk, defined as the blades' root mid-chord plane. Data was acquired at a sampling rate of 250 Hz while traversing the probe along 5 radial lines at a speed of $v_{tr} = 5$ mm/s. The radial lines were selected with an azimuthal spacing of 45° over a span of 180° for averaging out any potential asymmetries in the test setup while the extent of the radial sweep was limited to the range $r/R_p = [0.35, 1.2]$ (see Fig. 3). The recorded data were averaged every 0.4 s obtaining a spatial resolution Δr of 2 mm, corresponding to the probe's tip diameter. The mean total pressure distribution $p_t(r)$ obtained by averaging the radial lines was then used to estimate the thrust T produced by the propeller through integration [19]:

$$T = 2\pi \int_{R_n}^{R_p} \Delta p_t dr \approx 2\pi \sum_{i=1}^{N_p} \Delta p_{t_i} r_i \Delta r, \tag{3}$$

where $\Delta p_t = p_t - p_{t,\infty}$, N_p is the total number of sampling points in the radial direction, and r_i is the location of the i-th point with respect to the propeller's axis.

The turbulence intensity TI and the streamwise turbulence integral length scale Λ_x were retrieved through hot-wire-anemometry (HWA) involving a miniature single-wire probe (Dantec Dynamics 55P11) and a constant-temperature system (TSI IFA 300). Data was collected at a sampling frequency of 51.2 kHz for 40 s for 12 points along the $\theta = 90°$ radial line following a logarithmic distribution in the range $r/R_p = [0.35, 0.8]$ and a linear one in the range $r/R_p = [0.8, 1.1]$. The turbulence intensity TI (in [%]) is defined as [20]:

$$TI = \frac{v'_{rms}}{\bar{V}} \cdot 100 \tag{4}$$

where v'_{rms} is the root-mean-square of the velocity fluctuations and $\bar{V}$ is the average velocity component as retrieved by the hot-wire sensor. The integral turbulence length scale for the streamwise direction Λ_x is computed as [14]:

$$\Lambda_x = \bar{V} \int_0^\infty R_{xx}(\tau) d\tau, \tag{5}$$

where $R_{xx}(\tau)$ is the normalized autocorrelation function of the axial velocity and τ is the time delay interval. In practice, the first τ^* value for which R_{xx} reached a zero-crossing was used as a limit for the integration in Eq. (5).

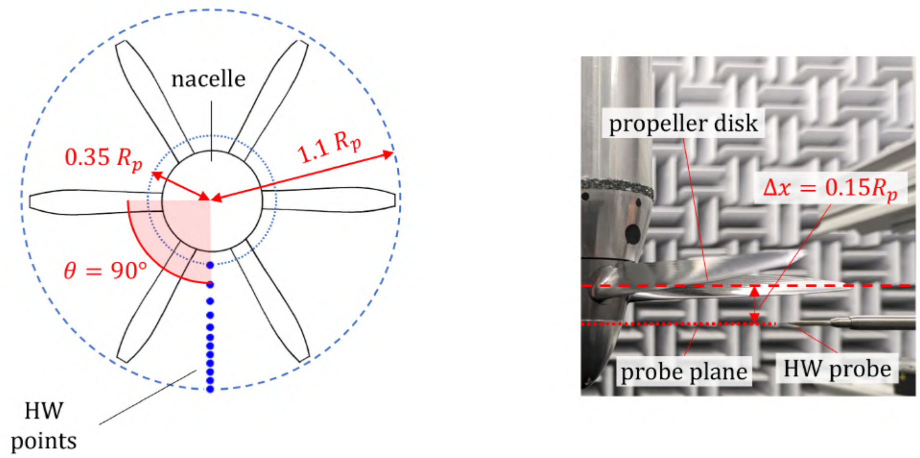

Fig. 4 Schematic of HWA measurement points as seen from downstream of the propeller (left) and lateral view of the relative position of the measurement plane with respect to the propeller (right).

2. Acoustic measurements

Acoustic measurements were performed employing a vertical polar arc for characterizing the directivity of the noise source and a planar, phased microphone array for spatial localization (Figure 5). The polar arc is equipped with 8 free-field 1/4-inch pre-amplified, high-frequency microphones (GRAS 46BE) at separation angles of 10° for a total window of 70°. A set of extension tubes allows placing the microphones at an adjustable distance from the support frame of the arc to reduce acoustic reflections. For the current case, the microphones were positioned at a radial distance of 1.3 m ($\approx 6.4D_p$) from the propeller's axis of rotation at the propeller's disk plane and such that a window covering 30° upstream and 40° downstream such plane was obtained. The phased microphone array instead consists of 64 GRAS 40PH free-field microphones arranged in a multi-arm spiral configuration with an elliptical shape 2-m long in the streamwise direction and 1-m wide in the lateral direction, which was optimised for source localization through beamforming [21]. All acoustic measurements were recorded synchronously for 60 s with a sampling frequency of 51.2 kHz.

D. Test matrix

Three different blade pitch angle settings $\beta_{0.7\ R_p}$ (i.e. the angle between the airfoil's mid-chord line and the propeller's rotational plane for the representative blade section located at $r = 0.7\ R_p$) were selected for the experimental campaign. Each $\beta_{0.7\ R_p}$ setting was tested with the three turbulence grids and a reference "grid off" case for a total of five combinations of tip Mach numbers M_{tip} and $\bar{V}$. An overview of the operating conditions of the propeller for each configuration is reported in Table 2. The tip Mach number M_{tip} is defined as:

$$M_{tip} = \frac{V_{r,tip}}{c_0} = \frac{\sqrt{(\Omega R_p)^2 + \bar{V}^2}}{c_0}, \tag{6}$$

where $V_{r,tip}$ is the relative flow velocity experienced by the blade tip and c_0 is the speed of sound at 16°C (289 K) and atmospheric pressure (101.325 kPa). In the same Table 2, the average inflow Mach number $\bar{M} = \bar{V}/c_0$, the blade passing

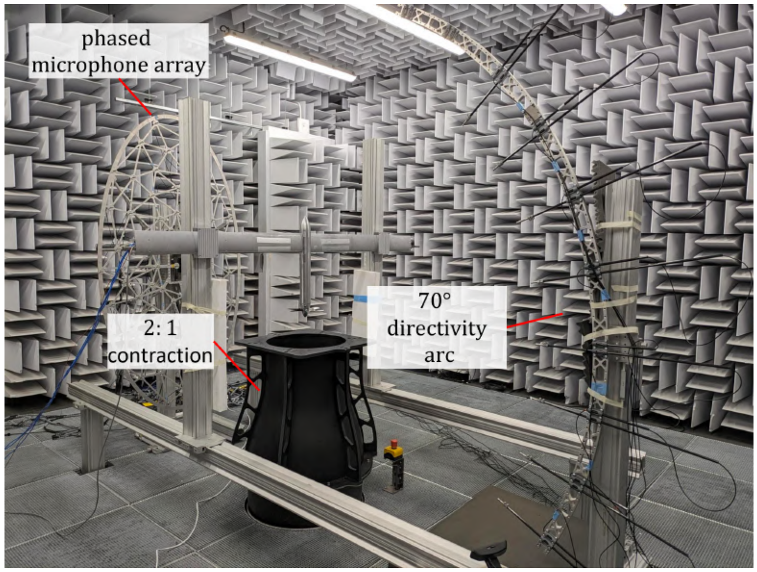

Fig. 5 Overview of the experimental setup for the acoustic measurements through a phased microphone array and a directivity arc spanning an azimuthal angle of $70°$ **in steps of** $10°$**.**

frequency $BPF = B\Omega/2\pi$ and the advance ratio $J = \bar{V}/nD_p$ are also reported. The choice of the tip Mach number M_{tip} as the main scaling variable was suggested by considering the "haystacking" parameter χ definition in Eq. (1). For a given inflow velocity and turbulence grid and if the stretching caused by the different thrust values produced by the propeller is neglected as a first approximation, the streamwise integral length scale Λ_x and the turbulence intensity remain relatively constant between different blade pitch angle settings $\beta_{0.7\ R_p}$. Keeping, therefore, a constant M_{tip} and, thus, a constant Ω translates then into a constant grid-specific χ for varying $\beta_{0.7\ R_p}$. Considering then the sound pressure level produced per unit of thrust allows accounting for the differences in thrust output caused by the different $\beta_{0.7R_p}$ settings. The thrust-scaled sound pressure level ($TSSP$) is defined as ([22, 23]):

$$TSSPL = 20 \log \frac{p_{rms}}{T/D_p^2}, \tag{7}$$

where p_{rms} is the root-mean-square value of the pressure fluctuations in a given frequency bandwidth Δf.

A preliminary characterization of the new nozzle, as well as of the turbulence grids, was also performed to obtain a reference condition for the measurements with the propeller mounted, an estimate of the values of the grid-dependent parameter χ, and, finally, to complement other studies on the use of grids in open-jet wind tunnels (e.g. [24], [25]).

Table 2 Propeller operating conditions investigated in the present study

$\beta_{0.7\ R_p}$ [deg]	Grids [-]	$\bar{V}$ [m/s]	$\bar{M}$ [-]	M_{tip} [-]	J [-]	BPF [Hz]
25, 30, 32.5	A, B, C, off	25	0.073	0.3	0.794	930.36
				0.325	0.730	1012.65
		30	0.088	0.3	0.967	917.19
				0.325	0.886	1000.56
				0.35	0.818	1083.41

III. Results and discussion

A. Characterisation of new nozzle and turbulence grids

A characterisation of the new contraction was first required for the selection of an appropriate distance from the contraction's exit at which to position the propeller's disk during the experimental campaign. To that end, both the average $\bar{V}$ and the fluctuating v' streamwise velocity profiles at the exit of the contraction were measured using HWA for different imposed freestream velocities $\bar{V}$ in the range from 20 m/s to 50 m/s, both with and without grids.

Figure 6 reports the average flow velocity and turbulence intensity profiles for different streamwise distances from the contraction's exit for $\bar{V}$ = 30 m/s and no grids installed. Similar trends were obtained for the other freestream velocities considered. It can be seen that while the overall average flow uniformity is conserved in all tested streamwise positions, the increasing values of the turbulence intensity TI due to the expanding shear layer of the free jet exiting the contraction imposes a limit on the position of the propeller to within the range $x = [0.2D_{ext}, 0.6D_{ext}]$. For the present study, the propeller's disk plane was set at a distance of $x = 0.4D_{ext}$ from the contraction's exit, with incoming turbulence intensity values lower than 0.1% for the baseline case of no grids installed.

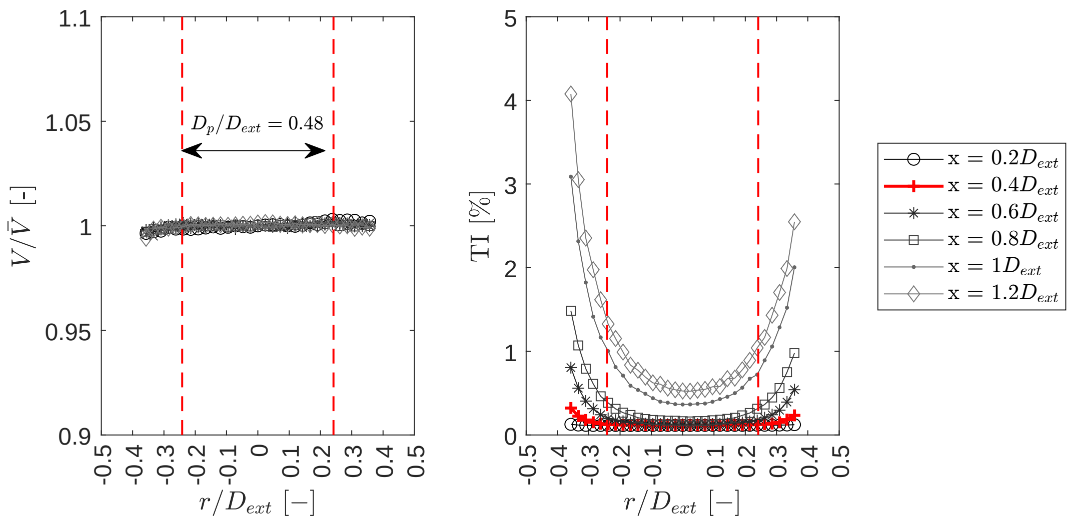

Fig. 6 Ratio of point-wise average and section-averaged streamwise velocity $V/\bar{V}$ (left) and turbulence intensity TI (right) profiles for an imposed freestream velocity $\bar{V}$ = 30 m/s and no turbulence grids installed. Red dashed lines indicate the limits of the propeller's area during the subsequent experimental campaign.

Figure 7 depicts the trends at the jet axis ($r/D_{ext} = 0$) and for increasing streamwise distances from its exit of both turbulence intensity TI and streamwise turbulence integral length scale Λ_x for the three different grids. The velocity fluctuations recorded with HWA were filtered *a posteriori* using a digital band-pass Butterworth filter of third order considering the frequency band from 20 Hz to 20 kHz as applied in previous works at the same facility [10]. Both quantities display the same qualitative behavior observed in similar studies on the subject (e.g. [14, 25]). In particular, Λ_x follows a linear increase until roughly $x/D_{ext} = 1$ from the contraction's exit, with a steeper growth until the end of the measured range ($x = 1.2D_{ext}$). Within the "linear" region, the coarser the mesh, the larger the turbulence integral length scales produced. The turbulence intensity TI shows, on the other hand, an exponential decrease from the contraction's exit, particularly evident for the coarsest grid (i.e. grid C). Similarly to Λ_x, the TI produced by the grids at any given streamwise location also increases with increasing mesh sizes. Table 1 reports the values of TI and Λ_x at the position chosen for the propeller plane.

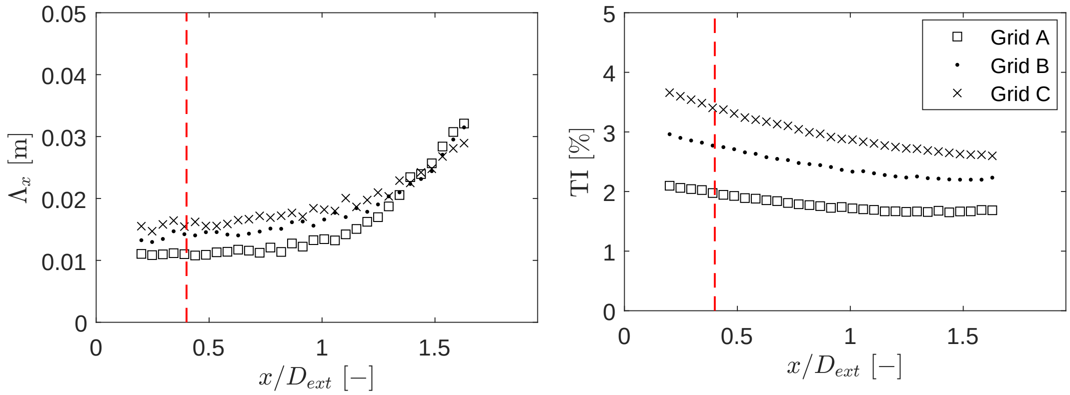

Fig. 7 Turbulence integral length scale Λ_x and turbulence intensity TI centerline streamwise distribution downstream of the contraction with installed turbulence grids for an imposed freestream velocity $\bar{V}$ = 30 m/s.

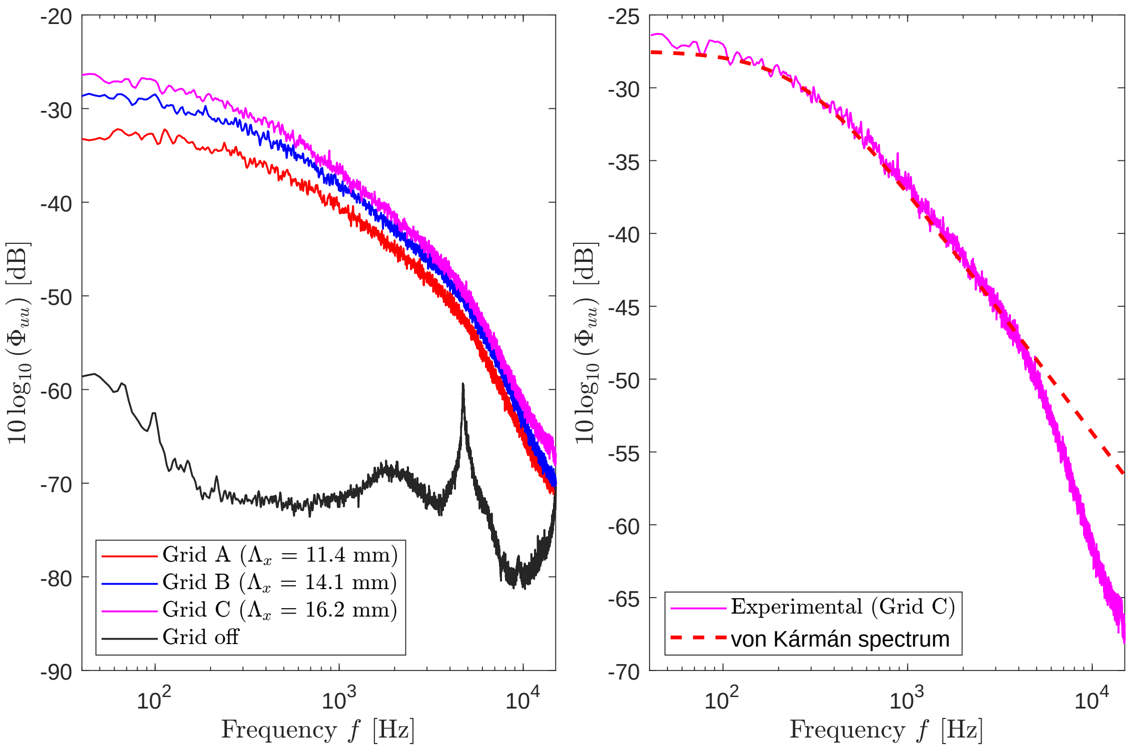

Fig. 8 Turbulence spectra for $\bar{V}$ = 30 m/s in the jet axis at $x = 0.4D_{ext}$ for grids on and grid off cases (left) and a close-up comparison between the von Kármán model and the experimental curve for grid C case (right). Frequency resolution Δf = 5 Hz.

The isotropy of the generated turbulence was evaluated by comparing the experimental velocity spectra Φ_{vv} with the von Kármán model for homogeneous and isotropic turbulence employing the integral turbulence length scale Λ_x experimentally obtained through Eq. (5). The von Kármán model for the spectral distribution of the velocity fluctuations is given by (e.g., [25]):

$$E(f) = \frac{4(v'_{rms})^2\Lambda_x}{\bar{V}} \frac{1}{\left[1 + (k_x/k_e)^2\right]^{5/6}}, \tag{8}$$

with:

$$\frac{k_x}{k_y} = 2\sqrt{\pi}\frac{\Gamma(1/3)}{\Gamma(5/6)}\frac{f\Lambda_x}{\bar{V}}, \tag{9}$$

where Γ is the gamma distribution. The spectra obtained both with and without turbulence grids at a point located on the jet axis at $x = 0.4D_{ext}$ from its exit for an average streamwise velocity of $\bar{V} = 30$ m/s are reported in the left plot of Figure 8. A comparison between the theoretical spectrum of Eq. (8) and that obtained for the coarsest grid (i.e., grid C) is also reported in the right of Figure 8. It can be seen that all grids follow the same qualitative trend as predicted by the von Kármán model for homogeneous, isotropic turbulence. In particular, the deviations occurring at higher frequencies (i.e., higher than ≈ 5 kHz) can be attributed to the spatial averaging of the smaller turbulence scales over the hot-wire's cross-stream length (1 mm), leading to an underestimation of the energy content at such scales [26].

B. Thrust production by isolated propeller

The effects of varying the blade pitch angle $\beta_{0.7\ R_p}$ while maintaining a constant inflow velocity ($\bar{V} = 30$ m/s) and tip Mach number ($M_{tip} = 0.35$) for the no-grid case and those corresponding to varying the turbulence grids for a constant blade pitch angle ($\beta_{0.7\ R_p} = 30°$), inflow velocity ($\bar{V} = 30$ m/s) and tip Mach number ($M_{tip} = 0.35$) on the total pressure coefficient C_{p_t} radial distribution at a distance of 0.2 R_p downstream of the propeller's disk are shown in Figure 9. The C_{p_t} coefficient is defined as [27]:

$$C_{p_t} = \frac{p_t - p_{t,\infty}}{q_\infty} + 1, \tag{10}$$

where $p_{t,\infty}$ and q_∞ are, respectively, the total and dynamic pressures of the incoming flow. It is clear from Fig. 9 how the total pressure distribution is highly dependent on the blade pitch angle setting $\beta_{0.7\ R_p}$, whereas it is only marginally affected by the turbulence levels produced by the three grids. In agreement with previous studies on the same propeller (e.g. [11]), the maximum pressure is generated at around $r = 0.75\ R_p$, with a shift towards higher radial values with increasing blade pitch angles.

Figure 10 reports the values of the thrust T computed through Eq. (3) for all the conditions tested. The thrust is expressed non-dimensionally in terms of the thrust coefficient T_c defined as:

$$T_c = \frac{T}{q_\infty A_p}, \tag{11}$$

where A_p is the propeller's disk area. As already noted above, it is clear how the presence of the grids does not alter the thrust produced by the propeller significantly. This observation will be of particular interest during the analysis of the acoustic results in Sec. III.D.

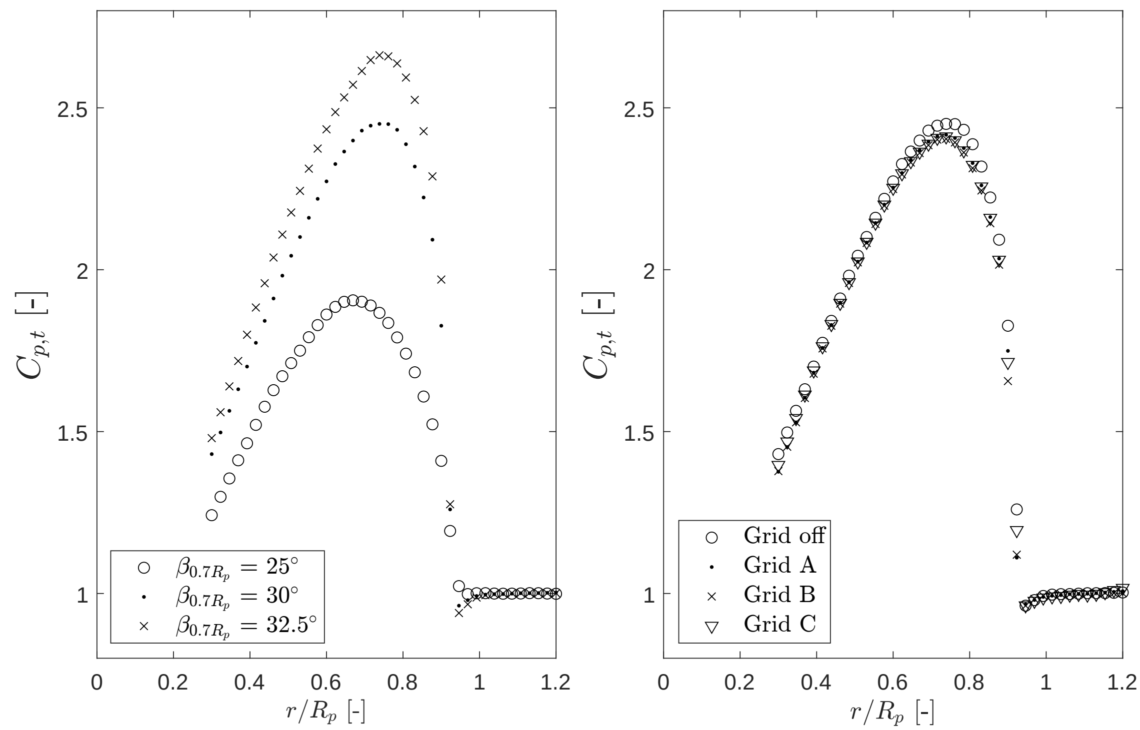

Fig. 9 Span-wise total pressure coefficient distribution at a distance of $0.2\ R_p$ downstream of the propeller's disk for varying collective pitch angles $\beta_{0.7\ R_p}$ at a constant inflow velocity ($\bar{V}$ = 30 m/s) and tip Mach number (M_{tip} = 0.35) (left) and for varying turbulence grid at a constant collective pitch angle ($\beta_{0.7\ R_p}$ = 30°), inflow velocity ($\bar{V}$ = 30 m/s), and tip Mach number (M_{tip} = 0.35) (right).

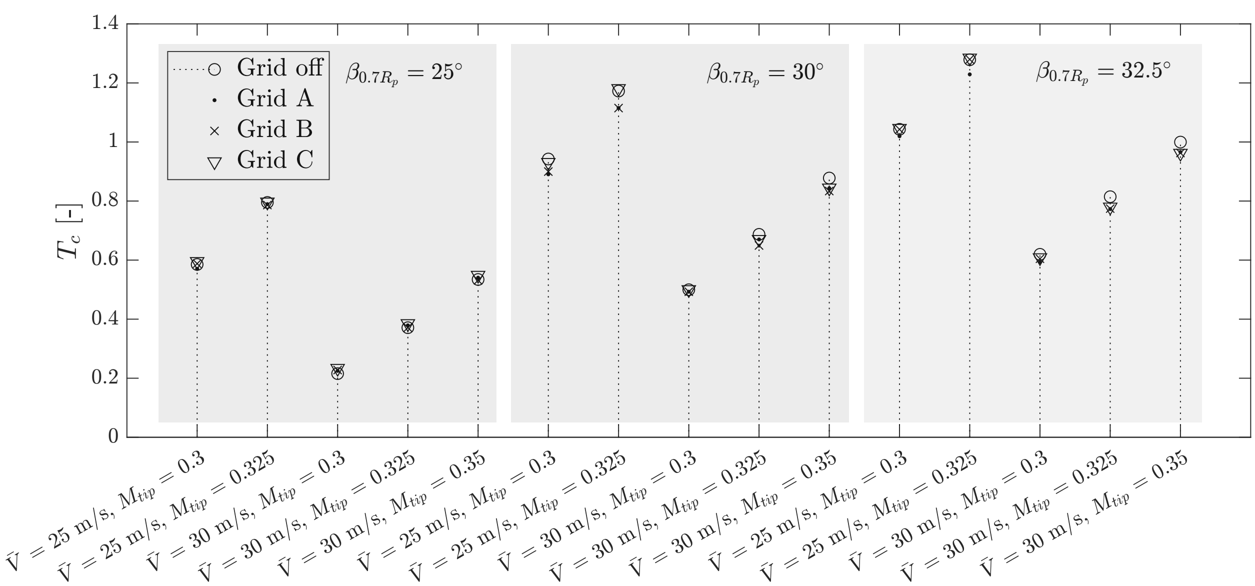

Fig. 10 Non-dimensional thrust coefficient T_c obtained for all configurations tested.

C. Ingested turbulence spectral characteristics

Figure 11 provides a comparison of the fluctuating streamwise velocity spectra at $r = 0.75\ R_p$ and at $0.15\ R_p$ upstream of the propeller for the case of a fixed blade pitch angle ($\beta_{0.7\ R_p}$ = 30°), tip Mach number (M_{tip} = 0.35), and average flow velocity ($\bar{V}$ = 30 m/s) for the different grids subject of the present study. The superposition of the turbulence spectrum obtained for the same grid (grid C) and average flow velocity ($\bar{V}$ = 30 m/s) with and without the propeller is also provided in Fig. 11. A particularly noticeable feature of the spectra are the sharp peaks at the BPF and its harmonics which are essentially independent from the level of turbulence in the incoming flow. These peaks are to be expected in the vicinity of the propeller's disk due to the periodic downwash caused by the passage of the blades over the hot-wire's location and constitute one of the hallmarks of propeller aerodynamics [28]. The superposition of the velocity spectrum for the coarsest grid at the same location with and without the presence of the propeller (right plot of Figure 11) shows how the overall shape of the streamwise ingested turbulence (except for the peaks at the BPFs) up to $0.15\ R_p$ upstream of the propeller disk is not greatly affected by the presence of the propeller and remains close to the von Kármán model for homogeneous and isotropic turbulence, especially in the energy-bearing lower frequency range.

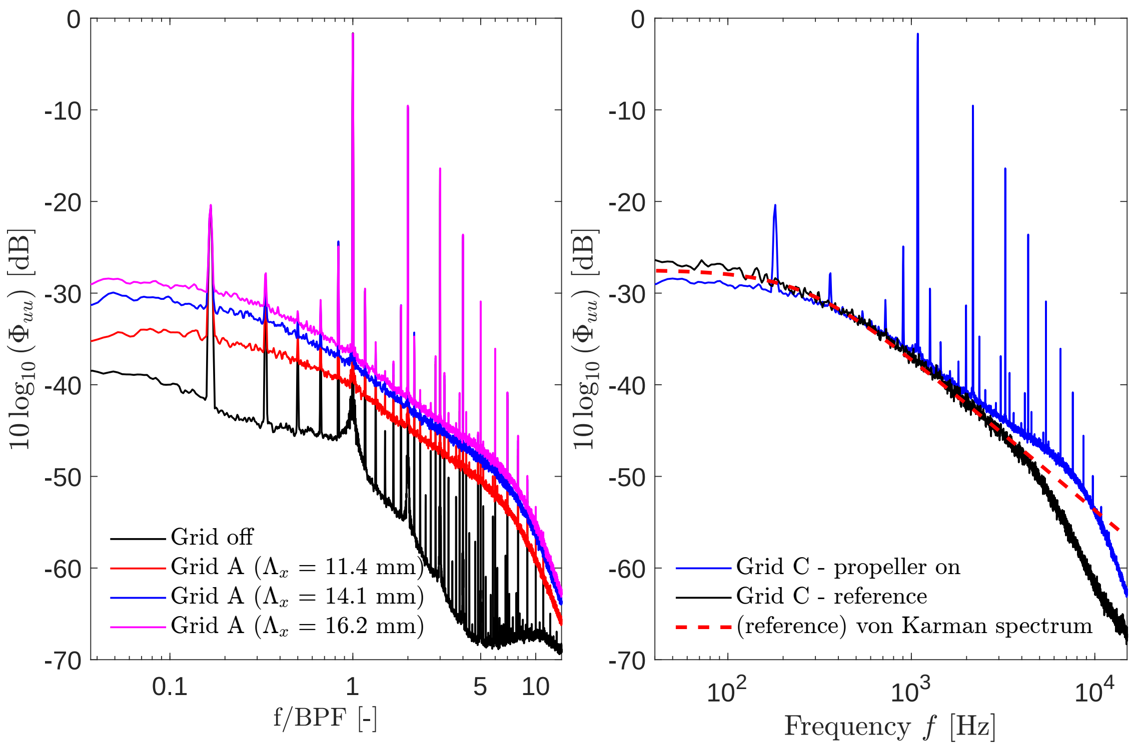

Fig. 11 Fluctuating streamwise velocity spectra for average flow velocity $\bar{V}$ = 30 m/s at $0.15\ R_p$ upstream of propeller disk and $r = 0.75\ R_p$ for grids on and grid off cases (left) and comparison between von Kármán model and experimental curve for grid C case (right) ($\beta_{0.7\ R_p} = 30°$, M_{tip} = 0.35, J = 0.818, $\Delta f = 5$ Hz).

Table 3 Chord-based Reynolds number $Re_{0.7\ R_p}$ and "haystacking" parameter χ values for the different turbulence grids (A, B, C) at all tested operational settings of the propeller.

$\bar{V}$ [m/s]	M_{tip} [-]	$Re_{0.7R_p}$ [-]	χ_A [-]	χ_B [-]	χ_C [-]
25	0.3	75479	2.67	3.30	3.83
	0.325	81413	2.90	3.59	4.17
30	0.3	76450	2.19	2.71	3.15
	0.325	82314	2.39	2.95	3.44
	0.35	88209	2.59	3.20	3.72

Whereas methods to filter out the BPF peaks (unrelated to the ingested turbulence) are possible (e.g., [29]), this shows that the turbulence length scales reported in 1 can still be employed as a first approximation for the estimation of the "haystacking" parameter χ of Eq. (1). Table 3 lists the values of this parameter for each turbulence grid for all the operational settings of the propeller. The chord-based Reynolds number $Re_{0.7\ R_p} = Vc/\nu$ for the representative blade section at $r = 0.7R_p$ is also reported for completeness.

D. Acoustic results

1. Single-microphone analysis

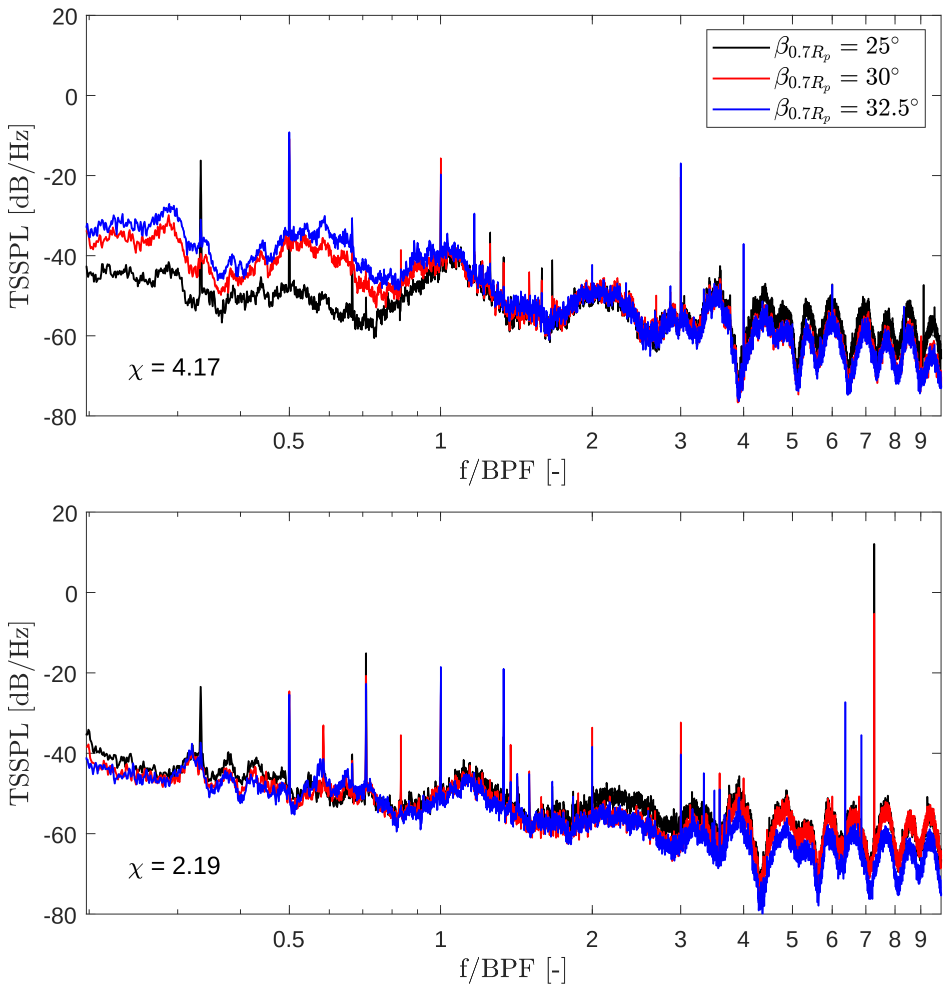

Fig. 12 Thrust-specific sound pressure level (TSSPL) for varying blade pitch angles for $\chi = 4.17$ (top) and for $\chi = 2.19$ (bottom) (Δf = 1 Hz).

The thrust-scaled spectra of the acoustic pressure for the three considered collective pitch angles as measured by a microphone from the polar arc located in the propeller's plane at a distance of 1.3 m ($\approx 6.4\ D_p$) from the propeller's rotational axis are shown in Fig. 12 for the cases of highest (top) and lowest (bottom) χ-TI values. Focusing on the former, it can be seen that the broadband acoustic energy content per unit of thrust generated is not strongly dependent on the blade pitch setting, except for frequencies lower than roughly the first BPF. In such a range, large differences between the lowest setting ($\beta_{0.7\ R_p} = 25°$) and the two higher ones ($\beta_{0.7\ R_p} = 30°$ and 32.5°) are present. At the lower χ-TI considered, these large differences disappear, leading to an even better collapse of the different curves.

A feature common to all spectra is the undulations particularly visible for frequencies higher than the third BPF. Such a phenomenon could be linked to set-up-specific filtering caused by the presence of the ducted grids. However, further analyses are necessary to confirm this hypothesis.

The effect on the produced thrust-specific acoustic energy (TSSPL) of sweeping through the different grid configurations for a constant pitch setting ($\beta_{0.7\ R_p} = 30°$), inflow velocity ($\bar{V} = 25$ m/s) and tip Mach number ($M_{tip} = 0.325$) is presented in Fig. 13. In general, an increase of the TSSPL for the broadband component is observed for increasing grid-generated turbulence intensities, especially for frequencies lower than the fifth BPF. Interestingly, however, the incoming turbulence has a non-negligible impact on the tonal emissions as well. The two subplots on the left of 13 report the differences in TSSPL for the first and third BPFs, respectively. Noise increases with respect to the no-grid case of up to 10 dB in the former and 6 dB in the latter are visible, with the grid producing the shortest turbulence length scale (grid A) generating the highest values of TSSPL.

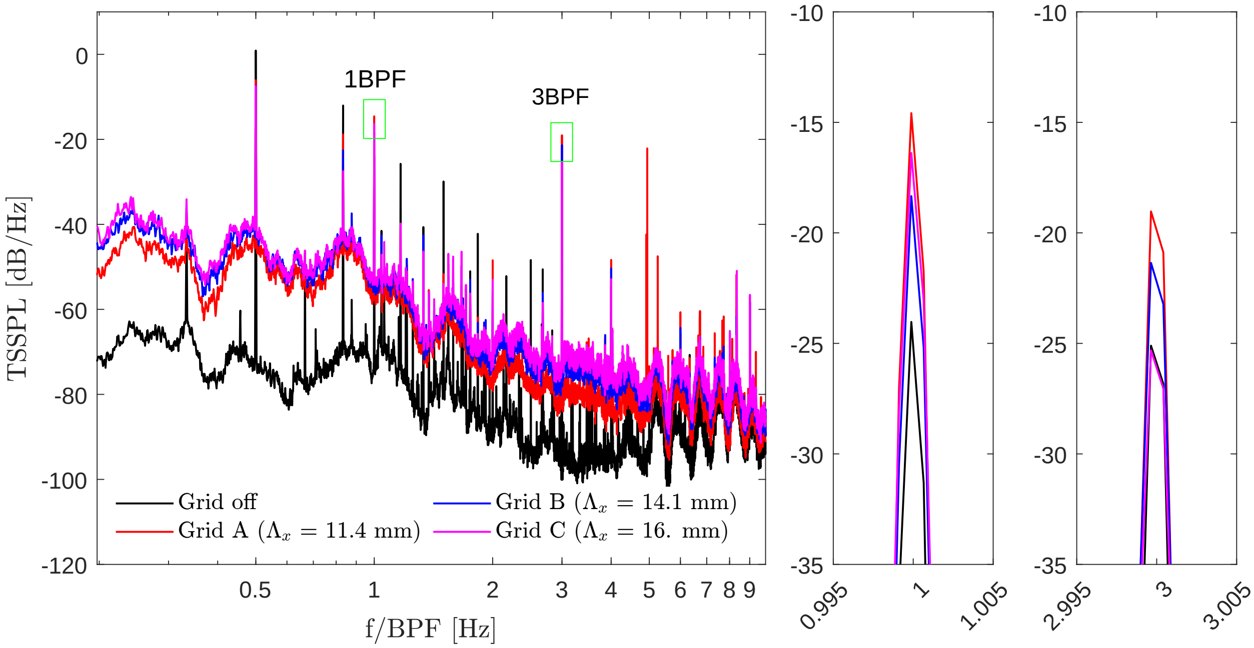

Fig. 13 Thrust-specific sound pressure level (TSSPL) for different grids (left) and particular of first and third BPFs (right) ($\beta_{0.7R_p}$ = 30°, $\bar{V}$ = 25 m/s, M_{tip} = 0.325, J = 0.73, Δf = 1 Hz).

2. Sound source directivity

The non-thrust-scaled directivity plots of some of the cases discussed above are reported in Fig. 14 in terms of the sound pressure level L_p per third-octave band (TOB) with center frequencies $f_c = 1000$ Hz and $f_c = 6300$ Hz. The first center frequency is chosen as the one most representative of the acoustic energy content distributed around the first BPF while the second one is more indicative of the acoustic energy contained within a frequency range dominated by the broadband component. Varying the collective pitch angle with a constant inflow turbulence is seen to greatly impact the sound level produced for the first BPF with the broadband component (6300 Hz) being only minimally affected. The incoming turbulence properties, instead, seem to have a non-negligible impact on both tonal and broadband components, as seen for the case of fixed blade pitch angle setting ($\beta_{0.7\ R_p} = 30°$) and advance ratio ($J = 0.73$). In particular, increasing values of the incoming turbulence intensity and integral length scales translate into higher noise emissions. The propeller noise also shows appreciable levels of directionality for both the center frequencies considered and the two comparisons discussed above, in line with other studies on the subject (e.g. [9, 30]). The addition of the grids is of particular importance to this aspect for the first BPF, especially downstream of the propeller, where a less pronounced cardiod-shaped pattern, typical of dipole-like sources, is observed.

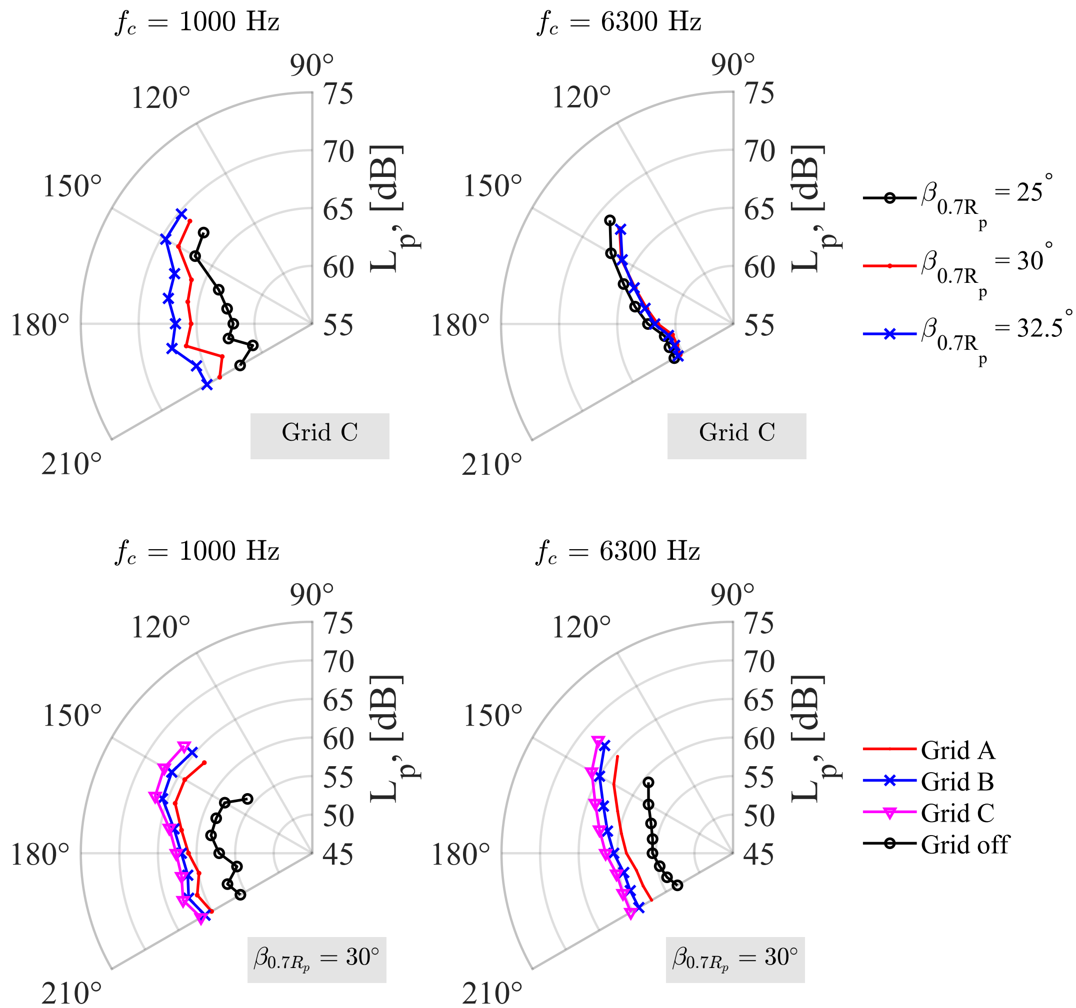

Fig. 14 Sound pressure level directivity plots per one-third-octave band for two center-frequencies (left: 1000 Hz and right: 6300 Hz) for selected configurations at a constant J = 0.73.

3. Sound source maps

The TOB acoustic source maps for the same center frequencies (1000 Hz and 6300 Hz) considered in the directivity analysis of III.D.2 are presented in Fig. 15 for the case of $\beta_{0.7\ R_p} = 30°$, $J = 0.73$ and incoming turbulence generated by the coarsest grid (i.e. grid C). The source maps are obtained by applying Conventional Frequency Domain Beamforming (CFDBF, e.g. [31]) with a scan grid with 20 mm spacing between neighboring points. It can be seen how the results are affected by the center frequency under consideration, with lower resolution for source localization at lower frequencies. Nonetheless, it is evident how at lower frequencies the wing-profiled sting holding the nacelle is an important source of noise (probably caused by vibration), while at higher frequencies, the propeller is the main sound source.

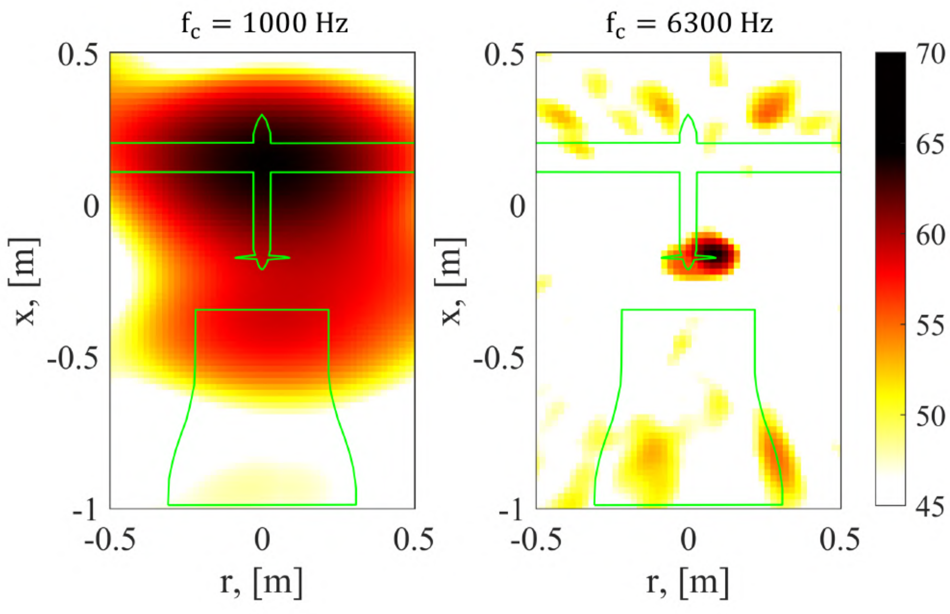

Fig. 15 TOB sound source maps per for two center-frequencies (left: 1000 Hz and right: 6300 Hz) with$\beta_{0.7\ R_p}$ = 30°, J = 0.73, grid C.

IV. Conclusions

The present paper reported on an aeroacoustic investigation of turbulence ingestion noise (TIN) generation by an isolated propeller for varying collective blade pitch angles and different turbulence conditions in an open-jet wind tunnel. The main results can be summarized as follows:

- square-mesh, square-bar grids can be used effectively in conjunction with an additional contraction for the generation of homogeneous, nearly-isotropic turbulence in open-jet wind tunnels;
- grid-generated turbulence ingestion does not impact appreciably the thrust produced by an isolated propeller for a fixed blade pitch angle;
- on the contrary, grid-generated turbulence ingestion greatly affects the noise produced by an isolated propeller, with a general increase in both broadband and tonal components and modifications of the source directivity pattern;
- "haystacking" does not seem to be a particularly important feature of grid-generated turbulence ingestion for this study's range of investigation.

Acknowledgments

The authors wish to thank Dr. Tomas Sinnige (Delft University of Technology) for his help in both devising a test matrix and in setting up the test rig for the experiments, Dr. Daniele Ragni (Delft University of Technology) for his contribution to the design of the new axisymmetric contraction and Ir. Perry Posthoorn (DEMO) for the manufacturing of part of the components employed in the set-up.

Funding Sources

This work is part of the HOPE (Hydrogen Optimized multi-fuel Propulsion system for clean and silEnt aircraft) project, and has received funding from the European Union's Horizon Europe research and innovation programme under grant agreement No. 101096275. Additionally, this publication is also a part of the *Listen to the future* project (project number 20247), a part of the Veni 2022 research programme (Domain Applied and Engineering Sciences). The latter project is granted to Roberto Merino-Martinez and is (partially) financed by the Dutch Research Council (NWO).

References

[1] Della Corte, B., Van Sluis, M., Veldhuis, L. L. M., and Gangoli Rao, A., "Power Balance Analysis Experiments on an Axisymmetric Fuselage with an Integrated Boundary-Layer-Ingesting Fan," *AIAA Journal*, Vol. 59, No. 12, 2021-12, pp. 5211–5224. https://doi.org/10.2514/1.J060570, URL https://arc.aiaa.org/doi/10.2514/1.J060570.

[2] Gunn, E. J., and Hall, C. A., "Aerodynamics of Boundary Layer Ingesting Fans," *Volume 1A: Aircraft Engine; Fans and Blowers*, American Society of Mechanical Engineers, 2014-06-16, p. V01AT01A024. https://doi.org/10.1115/GT2014-26142, URL https://asmedigitalcollection.asme.org/GT/proceedings/GT2014/45578/D%C3%BCsseldorf,%20Germany/240083.

[3] Glegg, S. A., Devenport, W., and Alexander, N., "Broadband rotor noise predictions using a time domain approach," *Journal of Sound and Vibration*, Vol. 335, 2015-01, pp. 115–124. https://doi.org/10.1016/j.jsv.2014.09.007, URL https://linkinghub.elsevier.com/retrieve/pii/S0022460X14007202.

[4] Hanson, D. B., "Spectrum of rotor noise caused by atmospheric turbulence," *The Journal of the Acoustical Society of America*, Vol. 56, No. 1, 1974-07-01, pp. 110–126. https://doi.org/10.1121/1.1903241, URL https://pubs.aip.org/jasa/article/56/1/110/677459/Spectrum-of-rotor-noise-caused-by-atmospheric.

[5] Alexander, W., Devenport, W. J., and Glegg, S. A., "Noise from a rotor ingesting a thick boundary layer and relation to measurements of ingested turbulence," *Journal of Sound and Vibration*, Vol. 409, 2017-11, pp. 227–240. https://doi.org/10.1016/j.jsv.2017.07.056, URL https://linkinghub.elsevier.com/retrieve/pii/S0022460X17305898.

[6] Zaman, I., Falsi, M., Zang, B., Azarpeyvand, M., and Camussi, R., "Experimental Parametric Investigation of the Haystacking Phenomenon for Propeller Boundary Layer Ingestion," *AIAA AVIATION 2023 Forum*, American Institute of Aeronautics and Astronautics, 2023-06-12. https://doi.org/10.2514/6.2023-4054, URL https://arc.aiaa.org/doi/10.2514/6.2023-4054.

[7] Zaman, I., Falsi, M., Zang, B., Azarpeyvand, M., and Camussi, R., "Effect of Tip Gap on Nearfield and Farfield Acoustics of Propeller Boundary Layer Ingestion," *AIAA AVIATION 2023 Forum*, American Institute of Aeronautics and Astronautics, 2023-06-12. https://doi.org/10.2514/6.2023-4055, URL https://arc.aiaa.org/doi/10.2514/6.2023-4055.

[8] Wojno, J. P., Mueller, T. J., and Blake, W. K., "Turbulence Ingestion Noise, Part 2: Rotor Aeroacoustic Response to Grid-Generated Turbulence," *AIAA Journal*, Vol. 40, No. 1, 2002-01, pp. 26–32. https://doi.org/10.2514/2.1637, URL https://arc.aiaa.org/doi/10.2514/2.1637.

[9] Jamaluddin, N. S., Celik, A., Baskaran, K., Rezgui, D., and Azarpeyvand, M., "Aeroacoustic Performance of Propellers in Turbulent Flow," *AIAA AVIATION 2021 FORUM*, American Institute of Aeronautics and Astronautics, 2021-08-02. https://doi.org/10.2514/6.2021-2188, URL https://arc.aiaa.org/doi/10.2514/6.2021-2188.

[10] Merino-Martínez, R., Rubio Carpio, A., Lima Pereira, L. T., Van Herk, S., Avallone, F., Ragni, D., and Kotsonis, M., "Aeroacoustic design and characterization of the 3D-printed, open-jet, anechoic wind tunnel of Delft University of Technology," *Applied Acoustics*, Vol. 170, 2020-12, p. 107504. https://doi.org/10.1016/j.apacoust.2020.107504, URL https://linkinghub.elsevier.com/retrieve/pii/S0003682X20306083.

[11] Van Arnhem, N., De Vries, R., Sinnige, T., Vos, R., Eitelberg, G., and Veldhuis, L. L. M., "Engineering Method to Estimate the Blade Loading of Propellers in Nonuniform Flow," *AIAA Journal*, Vol. 58, No. 12, 2020-12, pp. 5332–5346. https://doi.org/10.2514/1.J059485, URL https://arc.aiaa.org/doi/10.2514/1.J059485.

[12] De Vries, R., Van Arnhem, N., Sinnige, T., Vos, R., and Veldhuis, L. L., "Aerodynamic interaction between propellers of a distributed-propulsion system in forward flight," *Aerospace Science and Technology*, Vol. 118, 2021-11, p. 107009. https://doi.org/10.1016/j.ast.2021.107009, URL https://linkinghub.elsevier.com/retrieve/pii/S1270963821005198.

[13] Braslow, A. L., Hicks, R. M., and Harris Jr., R. V., "Use of grit–type boundary–layer transition trips on wind–tunnel models," Tech. Rep. NASA–TN–D–3579, NASA Technical Note (D–3579), September 1966. URL https://ntrs.nasa.gov/archive/nasa/casi.ntrs.nasa.gov/19660026829.pdf.

[14] Roach, P., "The generation of nearly isotropic turbulence by means of grids," *International Journal of Heat and Fluid Flow*, Vol. 8, No. 2, 1987-06, pp. 82–92. https://doi.org/10.1016/0142-727X(87)90001-4, URL https://linkinghub.elsevier.com/retrieve/pii/0142727X87900014.

[15] Livesey, J. L., and Laws, E. M., "Flow through non-uniform gauze screens," *Journal of Fluid Mechanics*, Vol. 59, No. 4, 1973-08-07, pp. 737–743. https://doi.org/10.1017/S0022112073001825, URL https://www.cambridge.org/core/product/identifier/S0022112073001825/type/journal_article.

[16] Bowen, L., Turhan, B., Kamliya Jawahar, H., Rezgui, D., and Azarpeyvand, M., "Aeroacoustic characteristics of distributed electric propulsion configuration with turbulent flows," *AIAA AVIATION 2023 Forum*, American Institute of Aeronautics and Astronautics, 2023-06-12. https://doi.org/10.2514/6.2023-4294, URL https://arc.aiaa.org/doi/10.2514/6.2023-4294.

[17] Bell, J., and Mehta, R., "Contraction Design for Small Low-Speed Wind Tunnels," , 1988.

[18] Morel, T., "Design of Two-Dimensional Wind Tunnel Contractions," *Journal of Fluids Engineering*, Vol. 99, No. 2, 1977-06-01, pp. 371–377. https://doi.org/10.1115/1.3448764, URL https://asmedigitalcollection.asme.org/fluidsengineering/article/99/2/371/413519/Design-of-TwoDimensional-Wind-Tunnel-Contractions.

[19] Malgoezar, A. M., Vieira, A., Snellen, M., Simons, D. G., and Veldhuis, L. L., "Experimental characterization of noise radiation from a ducted propeller of an unmanned aerial vehicle," *International Journal of Aeroacoustics*, Vol. 18, No. 4, 2019-07, pp. 372–391. https://doi.org/10.1177/1475472X19852952, URL http://journals.sagepub.com/doi/10.1177/1475472X19852952.

[20] Mayer, Y. D., Jawahar, H. K., Szőke, M., Ali, S. A. S., and Azarpeyvand, M., "Design and performance of an aeroacoustic wind tunnel facility at the University of Bristol," *Applied Acoustics*, Vol. 155, 2019-12, pp. 358–370. https://doi.org/10.1016/j.apacoust.2019.06.005, URL https://linkinghub.elsevier.com/retrieve/pii/S0003682X19301896.

[21] Luesutthiviboon, S., Malgoezar, A., Snellen, M., Sijtsma, P., and Simons, D., "Improving source discrimination performance by using an optimized acoustic array and adaptive high-resolution clean-sc beamforming," *Proceedings of the 7th Berlin Beamforming Conference*, 2018.

[22] Goyal, J., Sinnige, T., Avallone, F., and Ferreira, C., "Aerodynamic and Aeroacoustic Characteristics of an Isolated Propeller at Positive and Negative Thrust," *AIAA AVIATION 2021 FORUM*, American Institute of Aeronautics and Astronautics, 2021-08-02. https://doi.org/10.2514/6.2021-2187, URL https://arc.aiaa.org/doi/10.2514/6.2021-2187.

[23] Geng, X., Hu, T., Liu, P., Sinnige, T., and Eitelberg, G., "Analysis of Thrust-Scaled Acoustic Emissions of Aircraft Propellers and Their Dependence on Propulsive Efficiency," *ICAS-2021-0751*, 2021.

[24] Geyer, T. F., Poppe, W., and Sarradj, E., "Measurement of flow noise generation and pressure loss of nets and screens," *Applied Acoustics*, Vol. 134, 2018-05, pp. 69–74. https://doi.org/10.1016/j.apacoust.2018.01.008, URL https://linkinghub.elsevier.com/retrieve/pii/S0003682X1731099X.

[25] Bowen, L., Celik, A., Azarpeyvand, M., and Da Silva, C. R. I., "Grid Generated Turbulence for Aeroacoustic Facility," *AIAA Journal*, Vol. 60, No. 3, 2022-03, pp. 1833–1847. https://doi.org/10.2514/1.J060851, URL https://arc.aiaa.org/doi/10.2514/1.J060851.

[26] Sadeghi, H., Lavoie, P., and Pollard, A., "Effects of finite hot-wire spatial resolution on turbulence statistics and velocity spectra in a round turbulent free jet," *Experiments in Fluids*, Vol. 59, No. 3, 2018-03, p. 40. https://doi.org/10.1007/s00348-017-2486-8, URL http://link.springer.com/10.1007/s00348-017-2486-8.

[27] De Vries, R., "Hybrid-Electric Aircraft with Over-the-Wing Distributed Propulsion: Aerodynamic Performance and Conceptual Design," , 2022. https://doi.org/10.4233/UUID:EF87DC11-E7B2-4726-A41F-28588D64C58D, URL http://resolver.tudelft.nl/uuid:ef87dc11-e7b2-4726-a41f-28588d64c58d.

[28] Hanson, D. B., "Helicoidal Surface Theory for Harmonic Noise of Propellers in the Far Field," *AIAA Journal*, Vol. 18, No. 10, 1980-10, pp. 1213–1220. https://doi.org/10.2514/3.50873, URL https://arc.aiaa.org/doi/10.2514/3.50873.

[29] Go, S. T., Kingan, M. J., Bowen, L., and Azarpeyvand, M., "Noise of a shrouded propeller due to ingestion of grid-generated turbulence," *Journal of Sound and Vibration*, 2023-09, p. 118044. https://doi.org/10.1016/j.jsv.2023.118044, URL https://linkinghub.elsevier.com/retrieve/pii/S0022460X23004935.

[30] Ahmed, F., Zaman, I., Rezgui, D., and Azarpeyvand, M., "Aeroacoustics of a ducted fan ingesting an adverse pressure gradient boundary layer," *Journal of Fluid Mechanics*, Vol. 985, 2024-04-25, p. R1. https://doi.org/10.1017/jfm.2024.134, URL https://www.cambridge.org/core/product/identifier/S0022112024001344/type/journal_article.

[31] Sijtsma, P., "Phased Array Beamforming Applied to Wind Tunnel And Fly-Over Tests," 2010-10-17, pp. 2010–36–0514. https://doi.org/10.4271/2010-36-0514, URL https://www.sae.org/content/2010-36-0514/.